I. Pion Charge-Exchange at Fermilab, and

II. Some Remarks on Hadron Production at Large Transverse Momenta*

Morris Pripstein

Lawrence Berkeley Laboratory

University of California

Berkeley, California

Lectures delivered at the Canadian Institute of Particle Physics International Summer School, McGill University, Montreal, Canada June 16-21, 1975.

* Work done under the auspices of the U.S. Energy Research and Development Administration.

As may be implied from the titles, I will devote most of the discussion to the first topic and I will only touch briefly on the second. These topics are being explored experimentally at Fermilab and are part of a program to study neutral meson production under a variety of conditions at high energies, using very simple equipment, including a novel photon detector to detect these mesons via their purely photon decay modes. The first experiment, on pion charge-exchange, was performed by a collaboration from Caltech and LBL whose members are listed in Fig. 1a. For the subsequent experiments the collaboration has been augmented by a group from BNL and others from LBL (Fig. 1b).

I. Pion Charge-Exchange (CEX)

The perspective of the lecture is oriented to answering some of the general questions about the subject shown in Figure 2*. More specifically, I would like to provide an overview of an elegant and conceptually simple experiment recently completed at Fermilab to study pion charge-exchange (CEX) at beam momenta between 20 and 200 GeV/c. As part of this CEX overview, I shall first discuss the physics motivation and then describe the experiment, stressing the conceptual aspects. I will then proceed to discuss the results, which are still preliminary since we have not as yet completed our final estimates of some of the (small) corrections to be applied in the analysis. This will be done in the very near future. Preliminary results, at various stages of analysis, have already been reported.[1-3] The results to be presented here are essentially the same as those in Ref. 3 and include the entire data sample from 20 to 200 GeV/c.

---

* For those not familiar with Fermilab, the composite portrait of a particle physicist doing research there, depicted in Figure 2, is made up of the poet Allen Ginsberg (lower left) and actor-bon vivant W.C. Fields (lower right). The fellow at the top has been identified elsewhere.

I.A. Raison d'être or physics motivation.

The charge-exchange reaction,

$$\pi^- p \to \pi^0 n, \ \pi^0 \to 2\gamma \qquad (1)$$

is of compelling interest for at least two reasons, which I first list briefly and then elaborate on:

i) A measure of asymptopia: The cross section for reaction (1) in the forward direction is related to the difference between the $\pi^- p$ and $\pi^+ p$ total cross sections and its value is sensitive to small differences in these total cross sections. Thus, measurements of this forward cross section as a function of energy at high energies would provide a measure of the asymptotic behaviour of the $\pi^{\pm} p$ total cross sections; for example, are they approaching one another in value or is their difference becoming constant?

ii) Direct test of simple Regge theory: Reaction (1) and the reaction,

$$\pi^- p \to \eta n, \ \eta \to 2\gamma \qquad (2)$$

which is studied in the same experiment, are considered to be dominated at high energies by the exchange of a single Regge trajectory in each case. This represents a significant constraint on the predictions of the theory; hence, a measurement of the differential cross section of both reactions over a wide range of energies would provide a sensitive test of the Regge theory.

To elaborate, let me first derive in a simple and straightforward way the relationship between the forward CEX cross section and the difference in the $\pi^- p$ and $\pi^+ p$ total cross sections. To begin with, the forward CEX cross section is related to the CEX scattering amplitude in the usual way:

$$\left.\frac{d\sigma^{CEX}}{dt}\right|_{t=0} = \frac{\pi}{k^2}\left[(\mathrm{Re}\, A^{CEX})^2 + (\mathrm{Im}\, A^{CEX})^2 \right]_{t=0} \qquad \text{(Eq. 1a)}$$

$$= \frac{\pi}{k^2}(1 + R^2)\left[\mathrm{Im}\, A^{CEX}(0^\circ)\right]^2 \qquad \text{(Eq. 1b)}$$

Where A^{CEX} = CEX scattering amplitude

k = lab beam momentum

t = invariant 4-momentum-transfer

R = Re $A^{CEX}(0°)$/Im $A^{CEX}(0°)$

Now from isospin conservation,

$$A^{CEX} = \frac{1}{\sqrt{2}} (A^{+} - A^{-}) \qquad \text{(Eq. 2)}$$

Where $A^{\pm}$ = $\pi^{\pm}$ p elastic scattering amplitude.

Also, from the optical theorem,

$$\sigma_{total} = \frac{4\pi}{k} \text{ Im } A(0°) \qquad \text{(Eq. 3)}$$

Then, substituting equation (2) and (3) into (1), we obtain

$$\left.\frac{d\sigma^{CEX}}{dt}\right|_{t=0} = 25.5\ (1 + R^2)(\Delta\sigma)^2 \qquad \text{(Eq. 4)}$$

Where $\Delta\sigma = \sigma_{total}(\pi^{-}p) - \sigma_{total}(\pi^{+}p)$, and the constant on the right-hand side depends on the units used, which in this case are $d\sigma/dt$ in $\mu b/(GeV/c)^2$, k in GeV/c and $\Delta\sigma$ in mb. If R is unknown then equation (4) reduces to an inequality. However, as will be shown later, an estimate of R can be made from our data with some simple theoretical assumptions. Thus, equation (4) can be used to determine $\Delta\sigma$ from a measurement of $d\sigma^{CEX}/dt$ at $t = 0$.

It would now be instructive to compare the sensitivity in determining $\Delta\sigma$ from the charge-exchange measurement with that from measurements of the $\pi^{-}p$ and $\pi^{+}p$ total cross sections.

a) Error on $\Delta\sigma$ from CEX measurement:

From Eq. (4), $\left.\frac{d\sigma^{CEX}}{dt}\right|_{t=0}$ = constant·$(\Delta\sigma)^2$

Taking differentials, we get

$$\delta\ (d\sigma/dt) = \text{constant} \cdot 2 \cdot \Delta\sigma \cdot \delta\ (\Delta\sigma)$$

Then, the percentage error, α^{CEX}, in the CEX measurement is,

$$\alpha^{CEX} \equiv \frac{\delta\ (d\sigma/dt)}{d\sigma/dt} = \frac{2 \cdot \delta\ (\Delta\sigma)}{\Delta\sigma}$$

and therefore the error in $\Delta\sigma$ is

$$\delta\ (\Delta\sigma) = \frac{\Delta\sigma}{2} \cdot \alpha^{CEX} \qquad \text{(Eq. 5)}$$

b) Error on $\Delta\sigma$ from $\pi^{\pm}p$ total cross section measurements:

$$\Delta\sigma \equiv \sigma_t(\pi^- p) - \sigma_t(\pi^+ p) = \sigma_t^- - \sigma_t^+$$

$$\delta(\Delta\sigma) = \sqrt{(\delta\sigma_t^-)^2 + (\delta\sigma_t^+)^2}$$

$$= \sqrt{2}\ \delta(\sigma_t^{\pm}), \text{ since at high energies, } \sigma_t^- \simeq \sigma_t^+ = \sigma_t^{\pm}$$

Then, $$\delta(\Delta\sigma) = \sqrt{2}\ \sigma_t^{\pm} \cdot \alpha_t \qquad \text{(Eq.6)}$$

Where α_t = percentage error in the total cross section measurement.

Thus, to get the same error in $\Delta\sigma$ from both techniques, we need only compare equations (5) and (6),

$$\frac{\alpha^{CEX}}{\alpha_t} = \frac{2\sqrt{2}\ \sigma_t^{\pm}}{\Delta\sigma} \qquad \text{(Eq. 7)}$$

Recent measurements[4] at 100 GeV/c indicate $\sigma_t^{\pm} \simeq 24$ mb and $\Delta\sigma \simeq 0.7$ mb, so that according to equation (7), $\alpha^{CEX}/\alpha_t \simeq 100/1$. This means that, at 100 GeV/c, a 10% measurement of $d\sigma^{CEX}/dt(t = 0)$ is equivalent to a 0.1% measurement of both the $\pi^- p$ and $\pi^+ p$ total cross sections. As will be shown later, our CEX forward cross section measurements are certainly better than 10%.

With regard to tests of scattering theories at high energies, the most rigorous tests are provided from studies of reactions involving the fewest parameters—i.e.,

two-body reactions mediated by a single propagator. Two of the simplest such examples are the $n\pi^+$ and nn reactions (1 and 2). In each case, the final state has a spin-parity $J^P = 0^-$ meson and a nucleon as does the common initial state. The quantum numbers involved delimit the possible exchange propagators in the t channel. To illustrate, consider the general Feynman diagram in Fig. 3(a) for the case $\pi^- p \rightarrow$ neutral meson + neutron. First, since charge is exchanged then the propagator, X, must be charged so that its isotopic spin must be ≥ 1. Second, conservation of spin-parity at the (upper) meson vertex requires that X have parity $(-1)^J$ where J is the spin of X. Finally, because of G parity conservation at the meson vertex, X must have positive G parity in the CEX reaction (1) and negative G parity in reaction (2). These reasons then imply ρ-exchange in the former (Fig. 3b) and A_2-exchange in the latter (Fig. 3c). Simple Regge theory assumes the exchange of a single Regge trajectory in each case. However, polarization measurements[5,6] at lower energies suggest that the interactions are more complicated than the exchange of a single trajectory. Nonetheless, the indications are that the dominant contribution (even if not exclusively so) is still from the single exchange in each case.

In order to test further the Regge model predictions for these reactions it is important to study experimentally the two reactions at high energy over as large a range of energy and momentum transfer as possible. To this end, we have measured their differential cross sections at beam momenta of 20 to 200 GeV/c and in the range of four-momentum-transfer, $-t$, of 0 to ~ 1.4 $(\text{GeV}/c)^2$ for reaction (1) and to ~ 1.2 $(\text{GeV}/c)^2$ for reaction (2).

I.B. Experimental Method

Part of the beauty of this experiment, as I hope to demonstrate below, arises from the simplicity of the design of the set-up. As a consequence, the corrections to the raw data are small and are, for the most part, directly measured in the experiment.

The essential feature of the experiment is that the reactions

$$\pi^- p \to n\pi^\circ, \ \pi^\circ \to 2\gamma \qquad (1)$$

and

$$\pi^- p \to n\eta, \ \eta \to 2\gamma \qquad (2)$$

are identified by detection only of the two gamma rays from the meson decays and measurement of their kinematics. While the gamma-ray measurement resolution is certainly good enough to determine the kinematics of the parent meson, it is still not adequate to determine accurately the missing mass recoiling against the final-state meson as that of a neutron. To cleanly identify the final-state one needs additional constraints. Rather than attempt to detect the neutron, we have designed the experiment to reject all other final states. Thus, in general terms, the experiment consists of a liquid hydrogen target, a photon detector to measure the positions and energies of the two decay gamma rays and a carefully designed veto system of counters capable of vetoing not only charged particles which may be emitted form the target but also gamma rays from the π°'s produced in reactions other than the one of interest.

The basic performance requirements dictating the design of the apparatus are (a) excellent background rejection efficiency and (b) good resolution in the four-momentum-transfer t. These goals are non-trivial here. For example, at 100 GeV/c, the charge-exchange cross section is only about 3 μb whereas the $\pi^- p$ total cross section is about 24 mb and of which the total neutral final state cross section is about 30 μb. Thus the "signal" is approximately 10^{-4} of the $\pi^- p$ total cross section and 10^{-1} of the neutral final state cross section.

The t resolution has to be good enough so that we can extrapolate the CEX differential cross section, $d\sigma/dt$, reliably to zero degrees and to be sensitive to the dip structure at $-t \sim 0.6$ $(GeV/c)^2$ observed in lower energy experiments.[7-11] The apparatus was designed for the following resolution in t over the interval of interest, $-t = 0 - 1.5$ $(GeV/c)^2$:

at $-t =$	0.005	0.03	0.6	1.5 $(GeV/c)^2$
$\Delta t =$	0.0025	0.005	0.05	0.1 $(GeV/c)^2$

From these general objectives, we now proceed to show how the design of the apparatus follows in a logical, straightforward way.

i) Dimensions of the Photon Detector

From simple considerations of kinematics and geometry, we can first determine the detector position along the beam line with respect to the target, and its transverse dimensions. Once these are established then the target dimensions and the veto system design can be determined.

At high energies and small t ($-t \leq 2$ $[GeV/c]^2$) the γ rays from the π° or η decays tend to go forward in the lab at small angles, so that the detector can be small in size and yet have a large acceptance. In this region of energy and t,

$$-t \approx p^2\theta^2 \qquad \text{(Eq. 8)}$$

and

$$\theta^{\gamma\gamma}_{min} = \frac{2m}{p} \qquad \text{(Eq. 9)}$$

where θ is the π° or η production angle, p is the beam lab momentum, $\theta^{\gamma\gamma}_{min}$ is the minimum opening lab angle of the di-gamma system and m is the mass of the parent neutral meson (π° or η). Thus, for a given t, θ and $\theta^{\gamma\gamma}_{min}$ scale with beam momentum by the factor 1/p. Therefore, we let the detector position scale with beam momentum, making the distance between the detector and target, L, proportional to the beam

momentum as follows:

$$L = L_o \frac{p \text{ (in GeV/c)}}{100}, \qquad \text{(Eq. 10)}$$

where L_o = detector position at p = 100 GeV/c. L_o is then so chosen as to satisfy the following conditions: 1) the 2γ's must be well separated spatially at the detector so that they can be clearly resolved and 2) the detector should be kept as small as possible. L_o should also be consistent with the desired resolution in t and the di-gamma opening angle, determined by the spatial resolution of the γ-rays at the detector and the uncertainty in the interaction position in the hydrogen target. We will come back to this point later. For now, we consider the first condition. At high energies, the width of a converted γ-ray shower in the detector is about 1 cm. Then a conservative choice for the minimum spatial separation of the 2 γ's at the detector, $D^{\gamma\gamma}_{min}$, is about 4 cm, corresponding to a π^o decay at the minimum opening angle. Because of details in the construction of the detector, we actually chose $D^{\gamma\gamma}_{min} = 4.24$ cm. Therefore

$$\theta^{\gamma\gamma}_{min}(\pi^o) = \frac{2m_{\pi^o}}{p} = \frac{4.24}{L} \qquad \text{(Eq. 11)}$$

For p = 100 GeV/c, $L = L_o \simeq 16$ meters, from Eq. 11. Once the length has been chosen, the transverse dimensions are easily determined from the maximum t desired, using Eq. 8 and 9. For both the $n\pi^-$ and nn reactions (1 and 2) the desired $-t_{max} \sim 1.5$ $(GeV/c)^2$. Since the η's have a larger minimum decay opening angle than the π^o, the detector must be wide enough to detect the γ-rays from η's produced at $-t_{max}$. For 100 GeV/c η's, the detector at L_o = 16 meters must then have a radius greater than 29 cm, say 37 cm. We therefore make the detector rectangular, about 74 x 74 cm on a side.

ii) Target, Veto System and Experimental Layout

In order to maximize the yield of events and the target full-to-empty rate, the liquid hydrogen target should be as long as possible, consistent with the desired t-resolution. The uncertainty in the location of the interaction point in

the target contributes to the uncertainty in the scattering angle determination, and hence to the uncertainty in t. To minimize the variation in the t-resolution with beam momentum, in a practical way, our liquid hydrogen target consists of 2 cells, 20-and 40-cm long, to provide 3 target lengths -- 20, 40 and 60 cm.

The experimental arrangement is shown schematically in Figs. 4 and 5. The veto system consists of two parts -- a charged-particle veto surrounding the target which is used in the event trigger to define a neutral final state and an array of γ-ray shower counters which do not participate in the trigger logic but rather tag the presence of final-state γ-rays outside the acceptance of the γ-ray detector. The veto system was designed to satisfy the following requirements:

a) The system, including the γ-ray detector, should subtend > 99.99% of the entire 4π sr solid angle in the lab, for each lab momentum between 20 and 200 GeV/c;

b) The number of component parts of the system be kept at a minimum, consistent with the requirement of a simple geometry for each component, and (as emphasized earlier)

c) The detection efficienty should be sufficiently high (of course) so as to reject neutral-and charged-particle background down to levels of a few percent or better of the expected charge-exchange signal.

The charged-particle veto system consists of scintillation counters A_1, A_2 and A_3 surrounding the target (Fig. 4). Also surrounding the target is a system of γ-ray veto counters (called the "veto house") which was designed, particularly, to have a high detection efficiency for low energy γ-rays. The most serious background in this experiment comes from reaction such as $\pi^- p \to \pi^\circ N^*$ where the π° is indistinguishable from a valid charge-exchange π°. Detection of the low energy photons from the N* decay ($N^* \to n\pi^\circ$, $\pi^\circ \to 2\gamma$) identifies this reaction as background. The veto house shower counters are multi-layer lead-plastic sandwich counters, having eight lead plates for a total of five radiation lengths--the first four inner plates

are each 1/4 radiation length thick and the outer four are 1 radiation length each. this arrangement with two thicknesses of lead plates ensures a high detection efficiency for low energy photons, even for those incident at highly oblique angles. Instead of scintillator in the veto house we use a plastic Cerenkov detector (Pilot 425 in order to minimize the sensitivity to the recoil neutrons from true charge-exchange events.

The other shower veto counters upstream and downstream of the target, V_1 - V_4, are lead-scintillator sandwich counters having five lead plates totalling either 5 (as in V_1) or 10 radiation lengths. The positions and apertures of V_2, V_3 and V_4 vary with beam momentum so that they may still subtend all angles between those subtended by the detector in its new position and those subtended by the veto house which is fixed in position.

In addition to these counters, there is a plastic scintillator counter, A_4 (not shown in Fig. 4), which covers the aperture of V_4 and is used for tagging the presence of charged particles produced downstream from A_3 (such as from $K_s^\circ \to \pi^+\pi^-$ decays). To avoid potentially serious problems of backscattering from γ-ray showers in the detector, V_4 and A_4 are located far enough upstream (usually $\geq$ 2 m) from the detector so that the backscattered signal, if any, will have the wrong timing.

iii) The Photon Detector

Until now, we have only discussed the detector position and dimensions and then showed how the design of the rest of the system followed from those considerations. It is now appropriate to describe this novel detector which utilizes some "old-fashion" technology in a new scheme to measure accurately the π° or η kinematics.

The detector is basically a total absorption, lead-scintillator sandwich counter hodoscope, composed of 140 narrow "finger counters" that locate the shower position from the γ-ray conversion and integrate its total energy loss. Because counters are involved, the detector is capable of high counting rates. The more detailed description which follows is taken from our ref. 1.

The detector consists of a counter hodoscope array which measures the x and y (transverse coordinates) distributions of the energy deposited in one or more photon showers, integrated over the axial (incident beam direction) coordinate z. The detector is shown schematically in Fig. 6 (a,b). It is constructed of 19 lead plates, each 6.4 mm thick and 75 cm square. The plates are stacked normal to the direction of incident particles (z) with gaps between them of approximately 7 mm. These gaps are filled with long narrow scintillation fingers, 1.05 cm wide, which are close-packed and run the full width of the detector. Vertical and horizontal fingers are in successive gaps. The eight fingers having the same x coordinate or the same y coordinate are connected optically by curved light pipes at one end, and each set of eight fingers so connected constitutes one counter. There are 70 x-counters and 70 y-counters. Each finger has been separately wrapped with foil of graded reflectively, and a light trap captures those rays transmitted at large angles to the finger axis. Because of this special treatment, each counter yields pulses of uniform height (within 2%) over the entire counter length.

By simultaneously measuring all pulse heights, h_{xi} and h_{yi} $(1 \leq i \leq 70)$, in the detector counters it is possible to find the energy E, mass M, and production angle of a particle decaying at the target into the photons observed by the detector. The first three spatial moments of the pulse height distribution are given by

$$E_x = \sum_i h_{xi} \quad ; \quad E_y = \sum_i h_{yi} \qquad \text{(Eq. 12)}$$

$$\bar{x} = \frac{1}{E_x} \sum_i x_i h_{xi} \quad ; \quad \bar{y} = \frac{1}{E_y} \sum_i y_i h_{yi} \qquad \text{(Eq. 13)}$$

$$\overline{x^2} = \frac{1}{E_x} \sum_i x_i^2 h_{xi} \quad ; \quad \overline{y^2} = \frac{1}{E_y} \sum_i y_i^2 h_{yi} \qquad \text{(Eq. 14)}$$

E and M^2 are then evaluated from the spatial moments using the following

expressions:

$$E = \frac{1}{2}(E_x + E_y) \qquad \text{(Eq. 15)}$$

$$\left(\frac{M}{E}\right)^2 = \frac{1}{L^2}\left[(\overline{x^2} - \bar{x}^2) + (\overline{y^2} - \bar{y}^2) - 2\delta^2\right] \qquad \text{(Eq. 16)}$$

where L is the distance from the target to the detector and δ^2 is a constant which is an approximate measure of the inherent width of a single shower of half the total energy. The coordinates $(\bar{x}, \bar{y})$ are a good estimator of the point of intersection between the detector and the extrapolated trajectory of the decaying particle. The production angle is then computed from $(\bar{x}, \bar{y})$ and the π^- beam hodoscope information. These relations are based on the small angle approximation and hold for particles decaying in any decay orientation and into any number of photons as long as all of the photons enter the detector. The spatial resolution of the π° position extrapolated to the detector, is about 2.5 mm which allows for a sufficiently precise production angle determination consistent with the desired t-resolution for the CEX reaction.

I.C. Event Selection Criteria

The electronic trigger was a relatively loose one, basically requiring only that the final state be completely neutral. When this condition was satisfied, the information from all the counters was read into a computer and stored on magnetic tape for subsequent analysis. The off-line selection criteria used to define the data sample for reactions (1) and (2) are listed below.

1. The CLEAN requirement. There must be no pulse in any photon veto counter, thereby eliminating events with photons outside the solid angle of the detector.
2. Cerenkov Tag. A pulse in the threshold Cerenkov counter is required, thereby eliminating kaons and antiprotons from the beam flux.

3. Energy in the detector. The measured energy was required to be within the full energy peak corresponding to the incident π^- beam energy.

4. Number of photons. It was required that two individual showers be resolved by the detector for the charge exchange reaction.

5. Cosθ cut. In the decay $\pi^\circ \to \gamma\gamma$ (or $\eta \to 2\gamma$), the emission angle θ of the photons in the π° (or η) rest frame with respect to the π° (η) line-of-flight can be calculated from the data. Those events having emission angles with $|\cos\theta| > 0.7$ are eliminated because one photon has very small laboratory energy near $\cos\theta = 1.0$. This arbitrary cut is well outside the region where the detection efficiency falls below 100%.

6. Mass cut. The value of the mass M measured by the detector is required to be within the π° or η mass peak.

The distribution in M^2 for events satisfying criteria 1-5 (mass cut not imposed) is shown in Fig. 7 and 8(a). The level of the background outside the π° and η mass peaks is very low, permitting clean identification of the π° and η events. Moreover, the mass spectra for the one-photon and three-photon events exhibit no peak in the π° and η regions, indicating very little loss of events from the two-photon category.

As an illustration of other reactions which can be studied in the same experiment, we show the mass spectra for the three-photon ($N_\gamma = 3$) and $N_\gamma \geq 4$ events, subject to cuts 1-3 above. In the three-photon mass-squared spectrum (Fig. 8b) there is a distinct peak at $M^2 \sim 0.6\ (\mathrm{GeV}/c^2)^2$ corresponding to ω production in the reaction $\pi^- p \to n\omega$, $\omega \to \pi^\circ\gamma$. Even without constraining two out of the three γ's to have a π° mass, the signal-to-background is quite good. The mass spectrum for the higher γ- multiplicity events (Fig. 8c) shows a clear η signal (from $\eta \to 3\pi^\circ$ decays) and an enhancement in the region of the f° (or A_2, from $A_2 \to \eta\pi^\circ$).

While the overwhelmingly dominant effects in the di-gamma spectrum are the π^0 and η peaks, there is also a very small but clean peak at $M^2 \sim 0.9$ $(GeV/c^2)^2$ corresponding to $\eta'(959) \rightarrow 2\gamma$. In addition there is a small peak at $M^2 \sim 0.6$ which is due to $\omega \rightarrow \pi^0\gamma$ events in which our photon counting algorithm distinguishes only two out of the three photon showers. Improvements are being made in the algorithm which will significantly decrease even this small "feed-down" effect.

I.D. Results for the CEX Reaction $\pi^- p \rightarrow n\pi^0$

Plots of $d\sigma/dt$ versus $-t$ are shown in Fig. 9 and 10. The curves shown are hand-drawn and are for purposes of guiding the eye. In Fig. 11, the differential cross sections in the region of small t are displayed. There are between twenty and twenty-five thousand events for each momentum. The prominent features of the data are:

i) A characteristic forward peak with a dip at $t = 0$. The dip persists at all energies, but gets less pronounced with increasing energy;

ii) A break in $d\sigma/dt$ at $-t \sim 0.6$ $(GeV/c)^2$ for all energies. At the lowest energy, there is a dip at this value of t, followed by a secondary peak. As the energy increases, the height of this secondary peak gets progressively smaller, flattens out, and then becomes a shoulder on a falling distribution at the highest energy, and

iii) The forward peak exhibits shrinkage with increasing energy.

These features are evident also in the results from experiments at lower energies.[7-11] However the dip at $t = 0$ in our experiment is more pronounced than would be expected from the lower energy data. Furthermore, in the one experiment which overlaps ours in energy, by Bolotov et al,[8] the dip is essentially absent in their highest energy data at 48 GeV/c. The value of $d\sigma/dt$ at $t = 0$ was obtained by fitting the low t data to a second-order polynomial in t and then extrapolating the fitted curve to $t = 0$. The results are shown in Fig. 12, along with those of some other experiments. The disagreement with the data of Bolotov et al[8] is quite apparent.

The "total" charge-exchange cross section was obtained by integrating the differential cross section from -t of 0 to 1.5 $(GeV/c)^2$ and the results are shown in Fig. 13. Here, as in the case of $d\sigma/dt$ at $t = 0$, our results are systematically lower than those of Bolotov et al.[8] The discrepancy is one of normalization and of shape in $d\sigma/dt$ near $t = 0$. The curve in Fig. 13 is the result of a fit of our data and that of the CERN experiment[7] to an expression of the form

$$\sigma_T = A p_{lab}^{-N} \qquad \text{(Eq. 17)}$$

with $A = 719 \pm 11$ μb and $N = 1.175 \pm 0.004$. This fit spans the range from 5.9 to 200 GeV/c.

Let us now examine how some Regge theory predictions compare with our data. Our first preliminary results[1] from 20 to 101 GeV/c, based on a partial sample of the data, were reported at the 1974 London Conference and seemed to indicate deviation in some details of s and t-dependence from the prediction of the simple Regge pole model based on the original CERN data[7] in the beam momentum range 5-18 GeV/c. Figure 14 shows the forward differential cross sections for CERN data at 5.9 GeV/c[7] and our data at 40.6 and 101 GeV/c along with the Regge prediction (dashed curve) of Barger and Phillips,[12] and is reprinted from a theoretical paper by Desai and Stevens.[13] These authors[13] conclude from the observed discrepancy that a new mechanism may be responsible and provide their own hypothesis, which I won't go into here. Suffice it to say, first indications showed some discrepancy (Fig. 14) with the Barger-Phillips predictions.

With our entire data sample, at present, we determine a (preliminary) effective Regge ρ trajectory by fitting the differential cross sections to the functional form

$$\frac{d\sigma}{dt} = \frac{\beta(t)}{sq^2} \; s^{2\alpha(t)} \qquad \text{(Eq. 18)}$$

where $\alpha(t)$ and $\beta(t)$ are parameters to be determined as a function of t, q is the momentum of each particle in the cm system and s is square of the total cm energy.

An overall fit from 6 to 200 GeV/c was made, for various t-intervals, using the data from this experiment and from the CERN experiment.[7] Results of this fit are shown in Fig. 15 and 16. Figure 15 shows plots of $d\sigma/dt$ versus p_{lab} for several representative values of t with the curves from the fit to Eq. 18. Figure 16 shows the fitted values of $\alpha(t)$ versus t. The straight line corresponds to the best fit of the data to a linear expression in t. The linear hypothesis gives an acceptable fit, with a value of

$$\alpha_\rho(t) = 0.50 + 0.75t \qquad \text{(Eq. 19)}$$

Note that this result is still preliminary. When the final corrections to the data are made, the slope may change somewhat but the intercept will likely be unchanged. In any case, when the present fit is extrapolated to positive values of t, the straight line passes very close to the ρ pole, indicated by an asterisk on the plot. These results seem to be quite consistent with the simple Regge model description. What then of the descrepancies mentioned earlier? Recently, Barger and Phillips[14] refit the data, using their same $\rho + \rho'$ parametrization (the ρ' to account for the polarization) as before,[12] but including our London Conference data from 20 to 101 GeV/c. They quote a good fit to all the data and their results are compared to the $d\sigma/dt$ data in Fig. 17.[14] It should be noted that this comparison covers many orders of magnitude range in $d\sigma/dt$!

We now turn to the determination of $\Delta\sigma_t$, the difference in π^-p and π^+p total cross sections. If one assumes that the forward CEX scattering amplitude, $A^{CEX}(0)$, obeys a power law dependence on s, then from some general principles of axiomatic field theory (see, for example, Eden's book[15] on high energy collisions) one can derive the following relationship for R, the ratio of the real to the imaginary part of $A^{CEX}(0)$:

$$R = \tan \frac{\pi\alpha(0)}{2} \qquad \text{(Eq. 20)}$$

The power law assumption seems valid, as indicated by our results for $d\sigma/dt$ (t = 0) plotted in Fig. 12. The curve is a best fit of only our points to Eq. 18.

From our effective trajectory fit (Fig. 16 and Eq. 19), $\alpha(0) = 0.50$ so that $R = 1.00$ from the above expression. Plugging this into Eq. 4 and using the fit to our forward cross sections from Eq. 18, we obtain the curve for $\Delta\sigma_t$ versus p_{lab} shown in Fig. 18. For comparison, we also show the results from the recent total cross section measurements at Fermilab.[16] The curve from our determination of $\Delta\sigma_t$ appears to have a similar energy dependence to that exhibited by the total cross section points but the its normalization is somewhat lower, systematically, than the points.

I.E. Results for the Reaction $\pi^- p \to n\eta$ $(\eta \to 2\gamma)$

Figures 19 and 20 show the differential cross section results. The t-range $[-t < 1.2\ (\text{GeV/c})^2]$, is limited by statistics and not by the acceptance of the detector. As in the case of the π° data, the curves shown are hand-drawn and are to guide the eye. The prominent features of the forward peak are:

a) a dip at $t = 0$ which decreases in depth with increasing energy, and

b) a smooth exponential fall-off for $-t \geq 0.2\ (\text{GeV/c})^2$.

The integrated "total" cross section results are shown in Fig. 21, along with data from some lower energy experiments.[17,18] As for the $\pi^\circ n$ data, our data are systematically lower than those of Bolotov et al.[18] The curve shows the result of a fit to the same functional form as in Eq. 17.

An effective Regge A_2 trajectory was determined by fitting the differential cross section data to the same functional form as Eq. 18, using the data from the CERN experiment[17] as well as that from the present experiment. The results from the fit are shown in Fig. 22 which displays the plot of $\alpha(t)$ versus t. The straight line corresponds to the best fit of the data to a linear expression in t. The linear hypothesis gives an acceptable fit, with a value of

$$\alpha_{A_2}(t) = 0.40 + 0.68\ t \qquad \text{(Eq. 21)}$$

For purposes of comparison, Fig. 23 shows the effective A_2 trajectory from ref. 18. In order to get an acceptable fit, they require the trajectory (dashed curve) to have a quadratic form, with the trajectory turning over near $-t \sim 1.0$ $(GeV/c)^2$.

To conclude, I wish only to provide the reminder that for both the $\pi^0 n$ and ηn reactions, the signal at large $|t|$ is considerably smaller than at low $|t|$ so that the effects of background become increasingly important in this region, even for a "clean" experiment. We are still studying our own high-$|t|$ data for possible background effects even though they seem small. Needless to say, when assessing the trajectories reported from any of the charge-exchange experiments, consider the following first:

C A V E A T E M P T O R ! !

II. High Transverse Momentum Phenomena

High transverse momentum (P_T) phenomena are usually associated with interaction at a small distance. Thus, a study of hadron-nucleon collision P_T may provide important information about the structure of the nucleon. Recent results on the inclusive reactions.

$$pp \to \pi + \text{anything}, \qquad \text{at the ISR}^{19\text{-}21} \qquad (3)$$

and

$$pw \to \pi + \text{anything}, \qquad \text{at FNAL}^{22} \qquad (4)$$

show dramatic behaviour for $P_T \geq 3$ GeV/c, which suggests a new production phenomenon. At low P_T (≤ 1 GeV/c), the invariant cross section,

$$I = E \frac{d^3\sigma}{dp^3} \qquad \text{(Eq. 22)}$$

for single particle inclusive production (pions, kaons, protons, anti-protons) is of the form

$$I = e^{-6P_T} \qquad \text{(Eq. 23)}$$

The only hadronic theory which gives a prediction consistent with the behaviour of Eq. 23 is the thermodynamic model. At high P_T, the observed spectrum is quite different from this, as indicated for example by the π° yields at cm angle, θ^*, of 90° from the CERN-Columbia-Rockefeller (CCR) experiment[19] at the ISR. Their measurements of the invariant cross section versus P_T are shown in Fig. 24. The solid curve represents the best fit to the low P_T ($\leq$ 1 GeV/c) data, extrapolated to the high P_T region. At $P_T \simeq 3$ GeV/c, the yield is about 10^4 times greater than predicted from the e^{-6P_T} behaviour at low P_T. Another thing to note from the data in Fig. 24, is the variation with energy, $\sqrt{s}$. This data indicated a scaling behaviour at high P_T, with the invariant cross section having the form

$$E\frac{d^3\sigma}{dp^3} = A\,P_T^{-n}\,F(P_T/\sqrt{s},\ \theta^*) \qquad \text{(Eq. 24)}$$

How well this expression describes the CCR data is shown in Fig. 25, which is a plot of $P_T^n\ E\ d^3\sigma/dp^3$ versus $P_T/\sqrt{s}$, using a best fit value of $n = 8.24$. More quantitatively, the CCR group get a good fit to their data at $\theta^* = 90°$, with

$$E\frac{d^3\sigma}{dp^3} = \frac{15e^{-26P_T/\sqrt{s}}}{P_T^{8.2}}\ \text{mb}/(\text{GeV/c})^2, \qquad \text{(Eq. 25)}$$

A large number of theoretical models have been proposed in an attempt to explain the flattening out of the P_T spectrum at high P_T. A recent review of the various models is given by Ellis[23] at the London Conference. As a class, the so-called "hard-scattering" models (e.g. quark-parton models) predict invariant cross-sections of the form of Eq. 24 above. Perhaps anticipating the ISR results, Berman, Bjorken and Kogut[24] considered electromagnetic processes

(i.e., one-photon-exchange) and predicted hadron yields of the form $P_T^{-4}\ F(P_T/\sqrt{s})$. The P_T^{-8} dependence of the CCR data rules this out. On the other hand, models like the constituent exchange model of Blankenbecler, Brodsky and Gunion[25] do seem to describe the CCR data reasonably well. Even so, much more incisive experimental information is needed in order to determine which, if any, of the models provides the correct description of the high P_T phenomenon.

Until now, the experimental evidence of hadron production at high P_T comes only from nucleon-nucleon interactions. One extremely important and sensitive test of the various models is a comparison of the meson production at high P_T from πp and pp interactions. In the quark model description, the pion is made up of a quark-antiquark ($q\bar{q}$) pair whereas the proton consists of three quarks. Thus, the meson yields at high P_T can be quite different from πp and pp interactions.

To this end, we are carrying out another experiment at the Fermilab, using equipment from the CEX experiment, to make a detailed comparison of high-P_T (2-5 GeV/c) meson yields from the reactions

$$\pi^- p \rightarrow (\pi^0,\ \eta) + \text{anything} \qquad (5)$$

and

$$pp \rightarrow (\pi^0,\ \eta) + \text{anything} \qquad (6)$$

at 100 and 200 GeV/c. In addition, we will study the pp reaction (6) at 300 GeV/c in order to compare with results from ISR and Fermilab experiments on the same inclusive reaction at the same $\sqrt{s}$.

The experiment is characterized by the following important features:

i) the same set-up in one beam line measures both interactions. This tends to minimize systematic effects in making the comparison;

ii) both of the meson decay photons are detected (in contrast to experiments which detect only one photon);

iii) good spatial and energy resolution for the photon showers;

iv) good signal-to-noise (hopefully) as a result of ii) an iii);

v) wide kinematic region to be explored. In terms of the Feynman variable, $X_{||}$, the region to be covered by this experiment is, $X_{||} \sim 0 - 0.6$;

vi) with a liquid-hydrogen target, the normalization errors on the cross section measurements should be minimized.

The experiment uses the same equipment as in the CEX experiment except for all the veto counters (charged and neutral) which are removed. The detector is moved out of the beam line to one side at a non-zero lab angle corresponding to the desired $X_{||}$ region. Two settings of the detector position will cover the region of interest.

The event trigger in this experiment is much less restrictive than that in the CEX experiment and the data analysis is more difficult. We wish to trigger the apparatus whenever a group of γ-rays have a combined transverse momentum $\gtrsim$ 1.5 GeV/c (i.e., conservatively below the 3-5 GeV/c region of primary interest). To do so, we sum the pulse height from each vertical element, i, in the detector in such a way that the summed signal is approximately proportional to

$$\Sigma P_{Ti} = \Sigma P_i \sin\theta_i \propto \Sigma \text{ (weight)}_i \times \text{(Pulse height)}_i \qquad \text{(Eq. 26)}$$

If we associate an angle θ_i with respect to the beam for every vertical detector element, then each individual signal can be "weighted" by an amount proportional to sin θ_i, using an appropriate value attenuator. (This is only approximate since each vertical element subtends a range in θ along it length.)

The off-line data analysis is complicated by the presence of more than two photon showers and/or charged particles in the detector some of the time. As a result, the moments analysis used in the CEX experiment is not adequate here. Instead, we must identify and measure the position and energy of each shower by fitting a known shower shape to each peak in the detector. Preliminary results from some test runs are very encouraging. Fig. 26 shows the di-gamma mass spectrum

in the region of the π^0 for $pp \to 2\gamma$ + anything, at 300 GeV/c. Fig. 27 shows the same spectrum in the η mass region. The spectra show very clean π^0 and η peaks, respectively. For purposes of comparison, the inset in Fig. 27 shows the 2γ spectrum from the recent CCRS[26] experiment on the same inclusive reaction.

The major part of the data collection for our Fermilab experiment will start in August of this year. An added feature to the set-up will be second photon detector, cruder than the first one, which will be located on the other side of beam line from the original one to study correlations.

At present, the data from the short test runs on πp and pp are being analyzed but the analysis is still too preliminary to warrant any results on the π^0 and η yields to be included in these proceedings. Hopefully, though, the conceptual description of the experiment provided here will indicate the feasibility of achieving a good comparison of π^0 and η yields at high P_T from πp and pp interactions. Reliable results from this experiment should be forthcoming in the coming year.

References

1. A.V. Barnes, D.J. Mellema, A.V. Tollestrup, R.L. Walker, O.I. Dahl, R.A. Johnson, R.W. Kenney and M. Pripstein, LBL-3096 (1974); O.I. Dahl et al, LBL-3095 (1974). Both papers presented at the 17th International Conference on High Energy Physics, London, England, July 1-10, 1974.
2. R.L. Walker, Proceedings of the SLAC Summer Institute on Particle Physics, July 29-Aug. 10, 1974, SLAC-179, Volume II, p.1.
3. A.V. Tollestrup, invited talk at the Anaheim A.P. S. Meeting, Bull. Am. Phy. Soc., 20, No.1, p. 82, January, 1975.
4. A.S. Carroll et al, P.R.L. 33, 932 (1974).
5. D. Hill et al, Phys. Rev. Lett. 30, 239 (1973); D. Drobnis et al, Phys. Rev. Lett. 20, 274 (1968).
6. P. Bonamy et al, Nucl. Phys. B52, 392 (1973); P. Bonamy et al, Nucl. Phys. B16, 335 (1970); P. Bonamy et al, Phys. Lett. 23, 501 (1966).
7. A.V. Stirling et al, Phys. Rev. Lett. 14, 763 (1965); P. Sonderegger et al, Phys. Lett. 20, 75 (1966).
8. V.N. Bolotov et al, Nucl. Phys. B73, 365 (1974); V.N. Bolotov et al, Phys. Lett. 38B, 120 (1972).
9. I. Mannelli et al, Phys. Rev. Lett. 14, 408 (1965); M.A. Wahlig and I. Mannelli, Phys. Rev. 168, 1515 (1968).
10. M.A. Azimov et al, JETP Lett. 3, 216 (1966).
11. V.V. Barmin et al, JETP 19, 102 (1964).
12. V. Barger and R.J.N. Phillips, Phys. Rev. 187, 2210 (1969).
13. B.R. Desai and P.R. Stevens, pre rint CALT-68-457 (1974).
14. V. Barger and R.J.N. Phillips, Phys. Lett. 53B, 195 (1974).
15. R.J. Eden, High Energy Collisions of Elementary Particles, Cambridge University Press, 1967, pp. 194, 212.

16. A.S. Carroll et al, Phys. Rev. Lett. 33, 932 (1974); Orin Fackler, private communication.

17. O. Guisan et al, Phys. Lett. 18, 200 (1965).

18. V.N. Bolotov et al, Nucl. Phys. B73, 387 (1974).

19. F.W. Büsser et al, Phys. Lett. 46B, 471 (1973).

20. M. Banner et al, Phys. Lett. 44B, 537 (1973).

21. B. Alper et al, Phys. Lett. 44B, 521 (1973).

22. J.W. Cronin et al, Phys. Rev. Lett. 31, 1426 (1973).

23. S.D. Ellis, Proceedings of the XVIIth International Conference on High Energy Physics, London (1974), p. v-23.

24. S.M. Berman, J.D. Bjorken and J.B. Kogut, Phys. Rev. D4, 3388 (1971).

25. R. Blankenbecler, S.J. Brodsky and J.F. Gunion, Phys. Lett. 42B, 461 (1972); Phys. Rev. D6, 2652 (1972).

26. F.W. Büsser et al, Phys. Lett. 55B, 232 (1975).

Figure Captions

Fig. 1. Participants in the charge-exchange experiments at Fermilab.

Fig. 2. Composite portrait of a particle physicist.

Fig. 3. Feynman diagrams for various 2-body final states in $\pi^- p$ interactions.

Fig. 4. Schematic drawing of the experimental layout, showing all the counters in the setup. v-1, v-2, v-3, v-4 and the veto house comprise the γ-ray veto system. A_1, A_2 and A_3 constitute the charged particle veto system. M_1, M_2, M_3 are the beam telescope counters. H_1 and H_2 are beam hodoscope counters which measure the incident π^- position and angle. A_5 is a beam halo veto counter. $\check{C}$ is a threshold Cerenkov counter to tag the pions in the beam. Not shown is A_4, a plastic scintillator counter covering the aperture of v-4. Its function is to detect and flag charged particles produced downstream from A_3. The A_4 information is not used in the trigger.

Fig. 5. A perspective drawing of the experimental layout (not to scale). Details are given in Fig. 4.

Fig. 6. Schematic drawing of the photon detector. (a) Showing one of the 70 x counters and one of the 70 y counters. (b) Pictorial view showing the orientation of some of the constituent counters with their twisted light pipes.

Fig. 7. Mass squared spectrum of the 2-photon shower events in the region of the π^0 mass satisfying cuts 1-5 discussed in the text.

Fig. 8. Mass squared spectrum for different shower multiplicities in the detector a) $N_\gamma = 2$, for events satisfying cuts 1-5; b) $N_\gamma = 3$ and c) $N_\gamma = 4$. Events in b) and c) satisfy cuts 1-3.

Fig. 9. $d\sigma/dt$ ($\pi^- p \to \pi^0 n$) vs $-t$, for beam momenta of 20.7, 66 and 200 GeV/c. The curve through the 66 GeV/c data is hand-drawn, to guide the eye. Errors are statistical only.

Fig. 10. $d\sigma/dt$ ($\pi^- p \to \pi^0 n$) vs -t, for beam momenta of 40.6, 101 and 150 GeV/c. The curve through the 101 GeV/c data is hand-drawn, to guide the eye. Errors are statistical only.

Fig. 11. $d\sigma/dt$ ($\pi^- p \to \pi^0 n$) vs -t, in the region of small t. The errors shown are statistical only. Horizontal error bars at the bottom indicate values of Δt, the experimental t resolution at 101 GeV/c.

Fig. 12 $d\sigma/dt$ ($\pi^- p \to \pi^0 n$) at t = 0 versus beam lab momentum. The curve (described in the text) is a fit to the points of the present experiment only.

Fig. 13. Total integrated cross section ($\pi^- p \to \pi^0 n$) for $|t| \leq 1.5$ (GeV/c)^2 versus p_{lab}. The dark points are from the present experiment (Expt. 111). The curve is a fit to Eq. 17 using the data of CERN and this experiment.

Fig. 14. $d\sigma/dt$ ($\pi^- p \to \pi^0 n$) versus t in the low t region, showing the predictions from Barger and Phillips[12] (dashed curve) and those from Desai and Stevens.[13] This plot is reproduced from ref. 13.

Fig. 15. $d\sigma/dt$ ($\pi^- p \to \pi^0 n$) versus p_{lab} for various t values. The curves are from a fit to Eq. 18, using the CERN data and those from the present experiment.

Fig. 16. Effective trajectory for $\pi^- p \to \pi^0 n$. The asterisk is located at the position of the ρ pole.

Fig. 17. $d\sigma/dt$ ($\pi^- p \to \pi^0 n$) versus t, showing the results (solid curves) of the recent re-fit to the data by Barger and Phillips.[14] This plot is reproduced from their paper.

Fig. 18. The difference, $\Delta\sigma$, of the $\pi^- p$ and $\pi^+ p$ total cross sections, plotted as a function of p_{lab}. The solid curve is the "measure" of $\Delta\sigma$ from the present experiment. The points with error bars are from the total cross section measurements at Fermilab.[16]

Fig. 19. $d\sigma/dt$ ($\pi^- p \to n\eta$, $\eta \to 2\gamma$) versus -t, for 20.7, 66 and 200 GeV/c. The hand-drawn curve through the 66 GeV/c data is to guide the eye.

Fig. 20. $d\sigma/dt$ ($\pi^- p \to n\eta$), ($\eta \to 2\gamma$) versus $-t$, for 40.6, 101 and 150 GeV/c. The hand-drawn curve through the 101 GeV/c data is to guide the eye.

Fig. 21. Total integrated cross section ($\pi^- p \to n\eta$, $\eta \to 2\gamma$) for $|t| \leq 1.5$ $(GeV/c)^2$ versus P_{lab}. The curve is a fit to Eq. 17 using the data from CERN and the present experiment (Expt. 111).

Fig. 22. Effective trajectory for $\pi^- p \to n\eta$.

Fig. 23. Effective trajectory for $\pi^- p \to n\eta$ from the experiment of Bolotov et al.[18] The dark points are from a fit to CERN data and their own.

Fig. 24. CERN-Columbia-Rockefeller (CCR) results[19] on π° yields at large P_T in pp interactions. Invariant cross section versus P_T. The curve is an extrapolation of the low P_T (< 1 GeV/c) data.

Fig. 25. The function $F\ (P_T/\sqrt{s}) = P_T^n\ E\ (d^3\sigma/dp^3)$, as deduced from the CCR measurements,[19] using the best fit value of $n = 8.24$. Plot is reproduced from ref. 19.

Fig. 26. Mass-squared spectrum in the π° mass region of the di-gamma system for the reaction $pp \to 2\gamma$ + anything at 300 GeV/c, for 2γ events in the detector satisfying the following cuts: the decay $|\cos\theta^*_{\gamma\gamma}| \leq 0.7$ and $2.2 < P_T < 3.0$ GeV/c.

Fig. 27. Di-gamma mass-squared spectrum in the η mass region for the reaction $pp \to 2\gamma$ + anything, at 300 GeV/c. Same cuts as in Fig. 26. The inset shows the corresponding mass spectrum from the recent CCRS experiment[26] at the ISR.

A. PARTICIPANTS AND ESTEEMED COLLEAGUES IN THE PION CEX EXPERIMENT AT FERMILAB

FROM CALTECH	FROM LBL
Alan V. Barnes	Orin I. Dahl
D. Joel Mellema	Randy A. Johnson
Alvin V. Tollestrup	Robert W. Kenney
Robert L. Walker	Morris Pripstein

B. ADDITIONAL PARTICIPANTS AND ESTEEMED COLLEAGUES IN THE HIGH-P_T EXPERIMENT

FROM BNL	FROM LBL
Greg Donaldson	
Howard Gordon	Art Ogawa
Kwan-Wu Lai	Steve Shannon
Iulio Stumer	

Figure 1

XBB 7410-7470A

Fig. 2

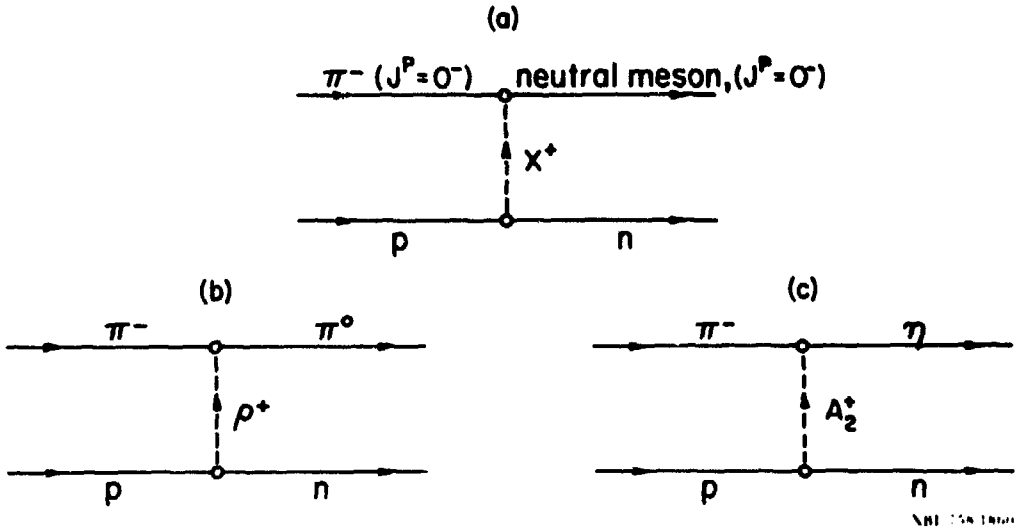

Fig. 3

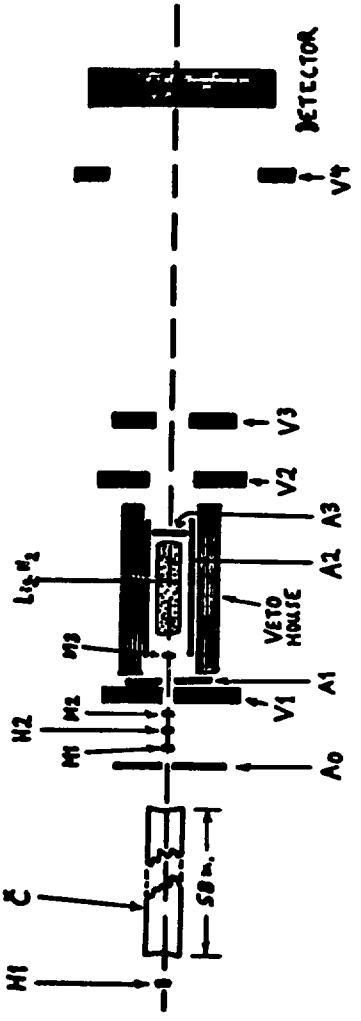

Fig. 4

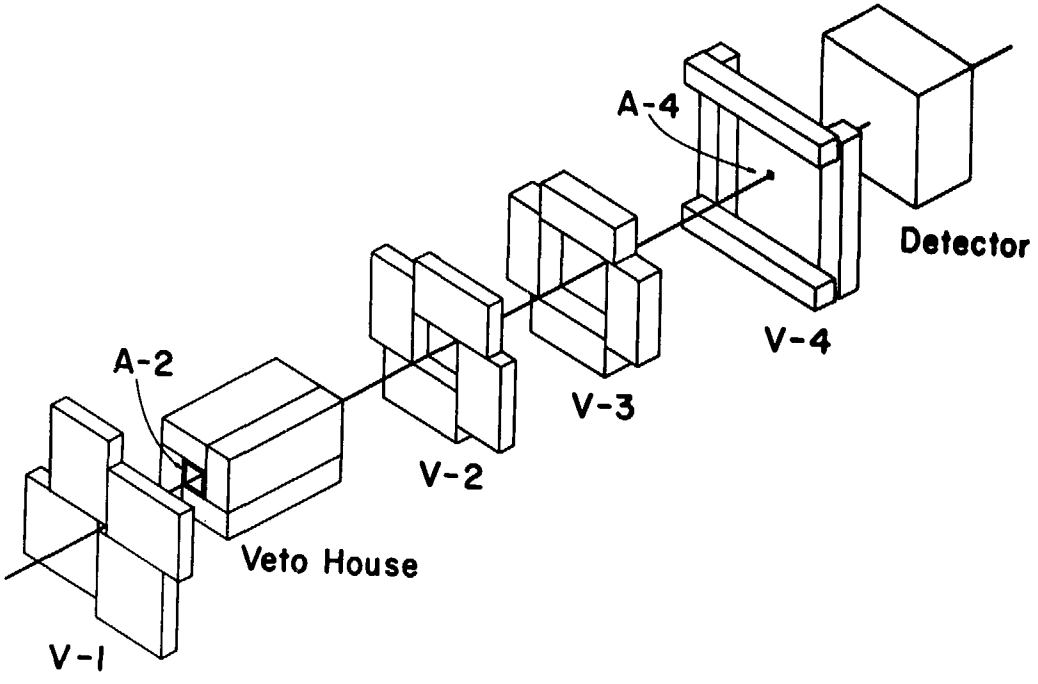

NBL 757-1849

Fig. 5

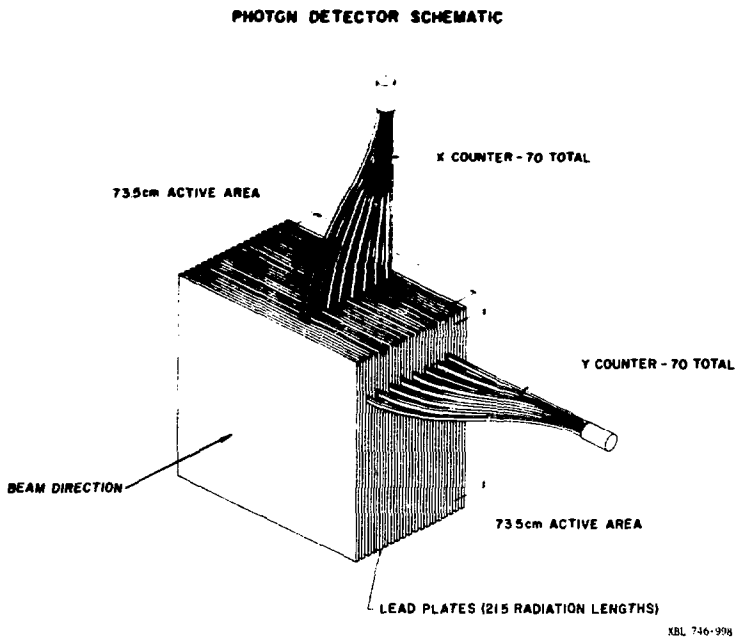
PHOTON DETECTOR SCHEMATIC
X COUNTER - 70 TOTAL
73.5cm ACTIVE AREA
Y COUNTER - 70 TOTAL
BEAM DIRECTION
73.5cm ACTIVE AREA
LEAD PLATES (21.5 RADIATION LENGTHS)
XBL 746-998

Fig. 6(a)

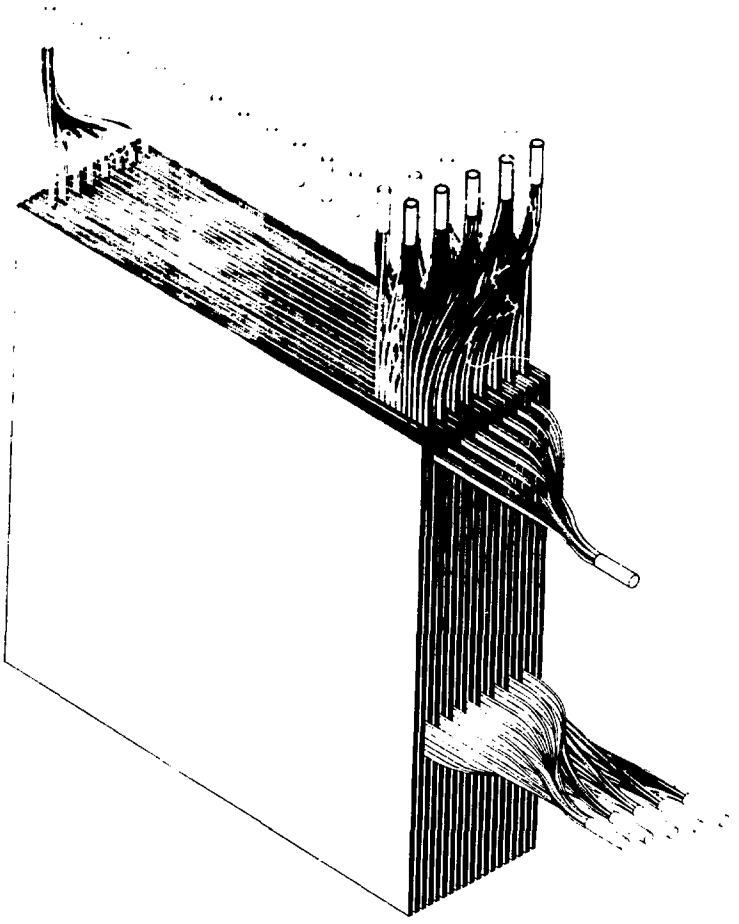

NBL 757-1845

Fig. 6(b)

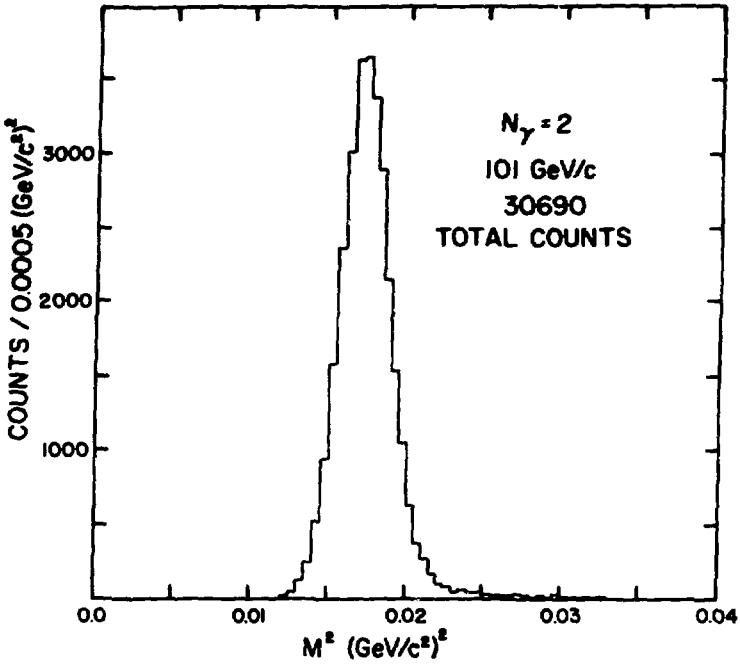

XBL 757-1851

Fig. 7

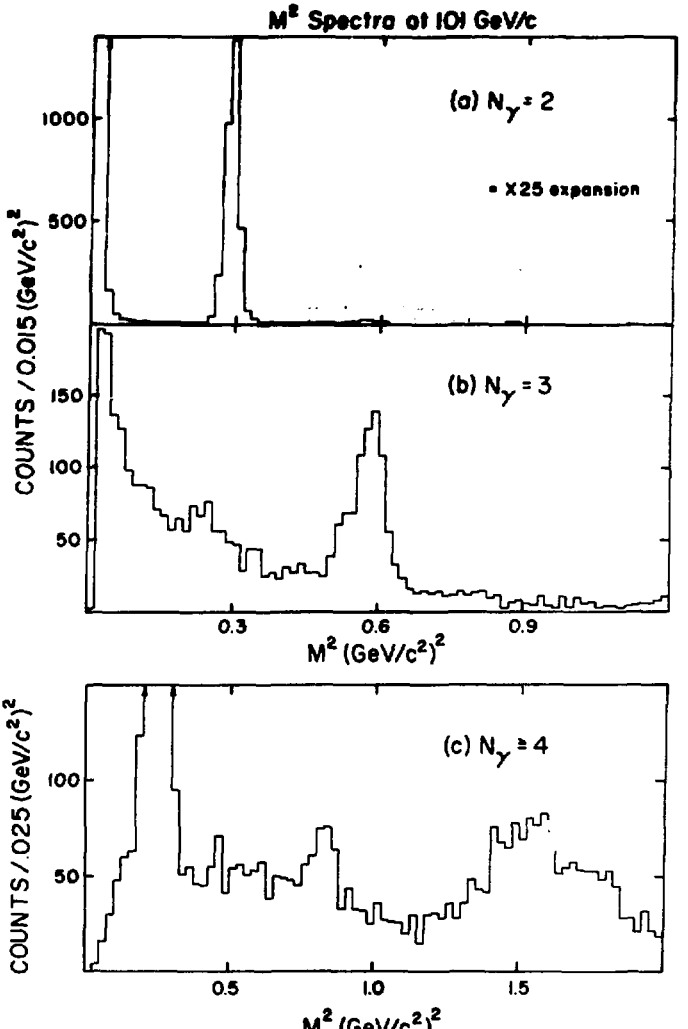

XBL 757-1850

Fig. 8

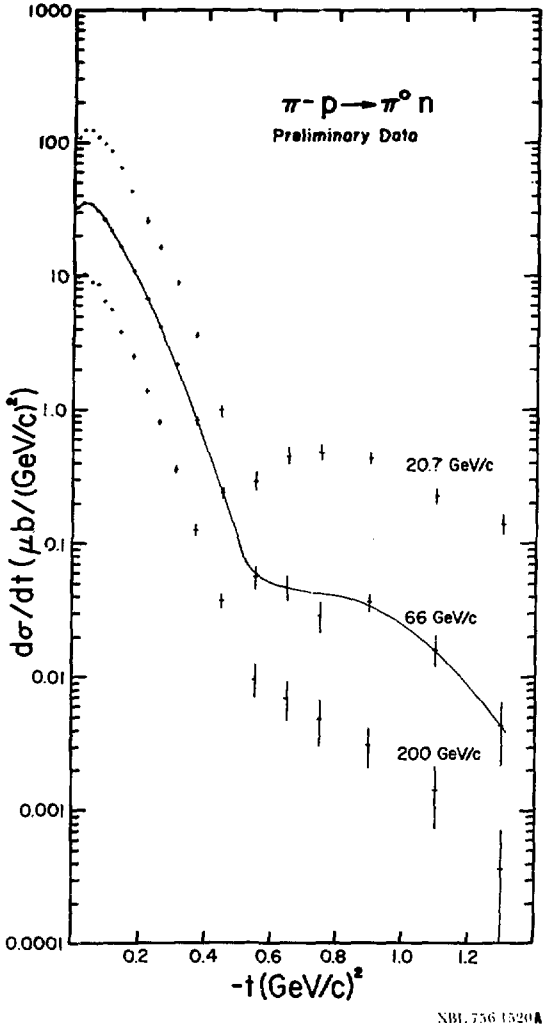
$\pi^- p \rightarrow \pi^0 n$
Preliminary Data
20.7 GeV/c
66 GeV/c
200 GeV/c
$d\sigma/dt\ (\mu b/(GeV/c)^2)$
$-t\ (GeV/c)^2$
1000
100
10
1.0
0.1
0.01
0.001
0.0001
0.2
0.4
0.6
0.8
1.0
1.2
NBL 756 1520A

Fig. 9

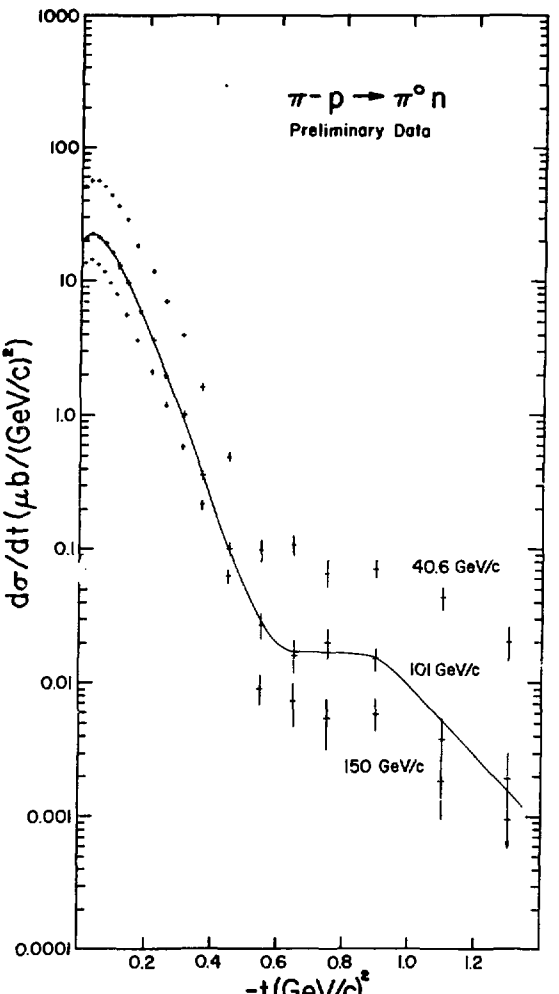
π⁻ p → π° n
Preliminary Data
40.6 GeV/c
101 GeV/c
150 GeV/c
dσ/dt (μb/(GeV/c)²)
-t(GeV/c)²
1000
100
10
1.0
0.1
0.01
0.001
0.0001
0.2
0.4
0.6
0.8
1.0
1.2
XBL 756-1518A

Fig. 10

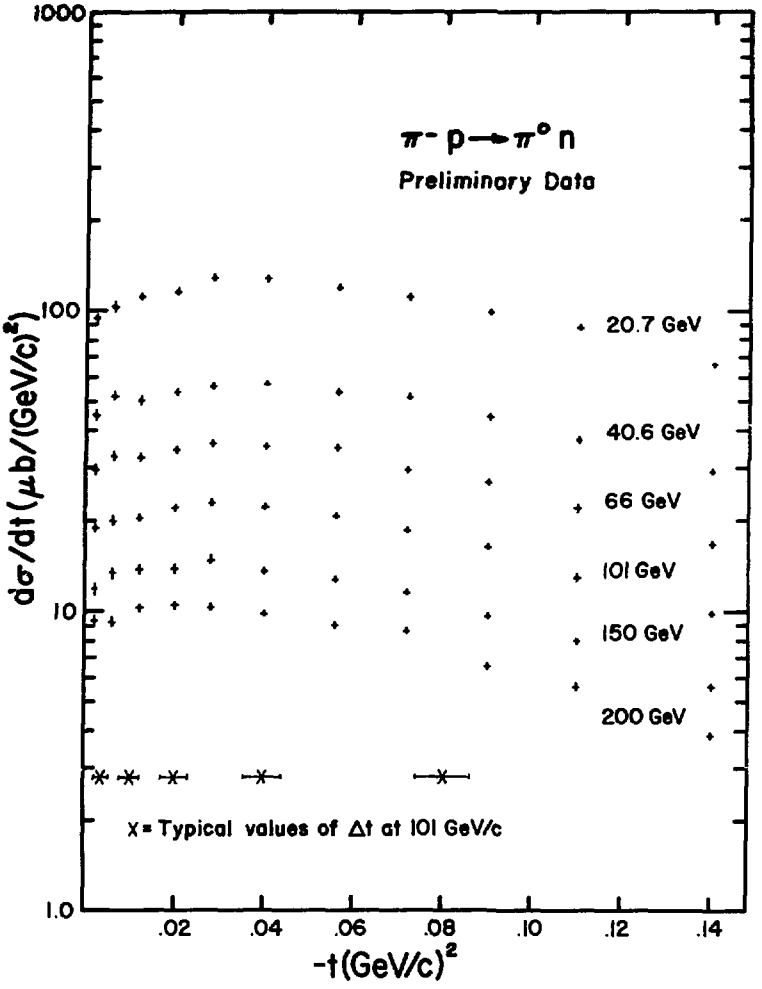

XBL 756-5513A

Fig. 11

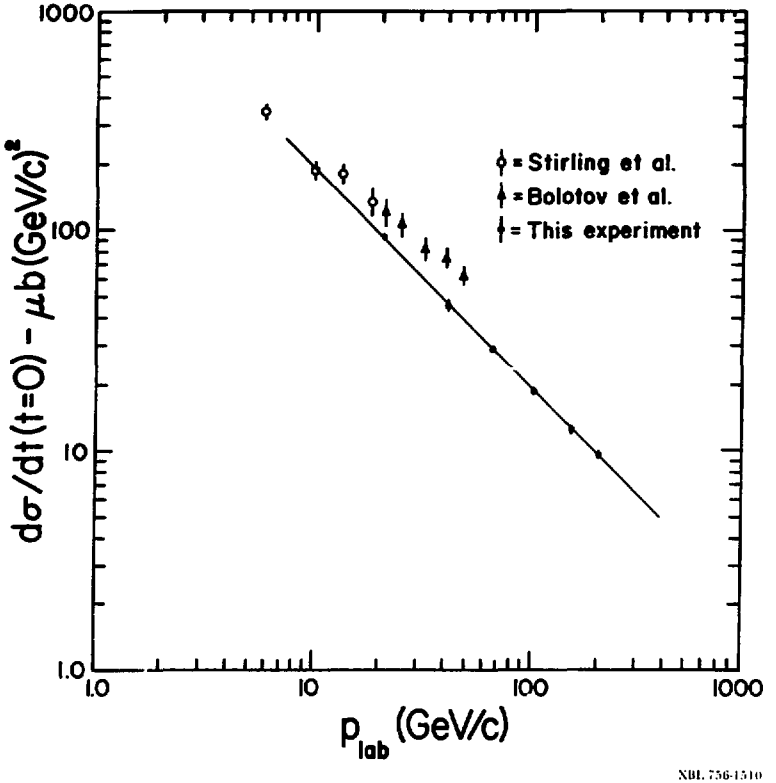
1000
100
10
1.0
1.0
10
100
1000
dσ/dt(t=0) - μb(GeV/c)²
p_lab (GeV/c)
= Stirling et al.
= Bolotov et al.
= This experiment
NBL 756-1510

Fig. 12

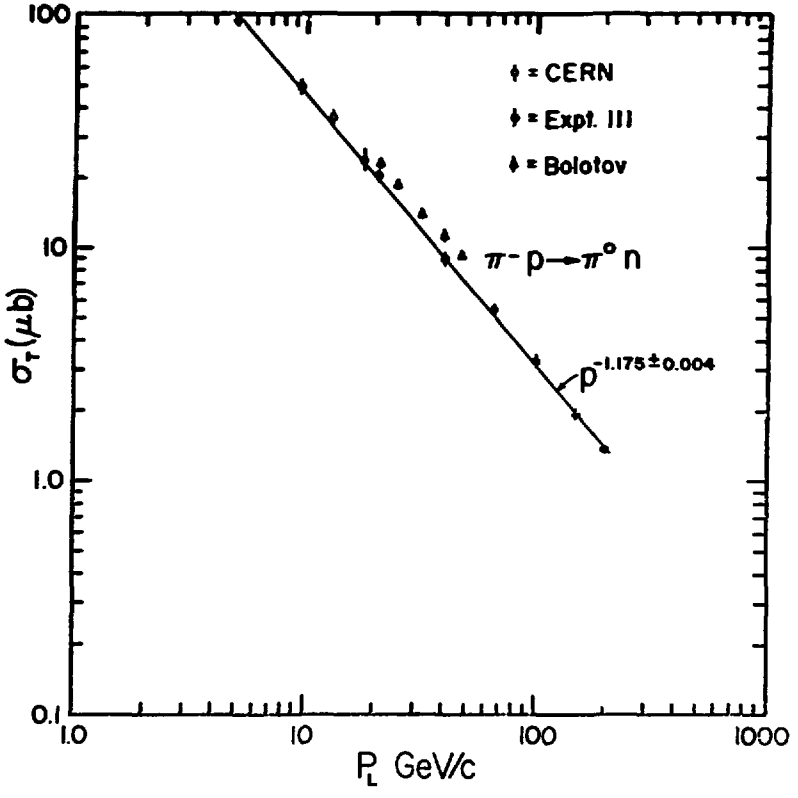
100
10
1.0
0.1
1.0
10
100
1000
σ_T (μb)
P_L GeV/c
♦ = CERN
♦ = Expt. III
♦ = Bolotov
$\pi^- p \rightarrow \pi^0 n$
$p^{-1.175 \pm 0.004}$
NBL 757-1847

Fig. 13

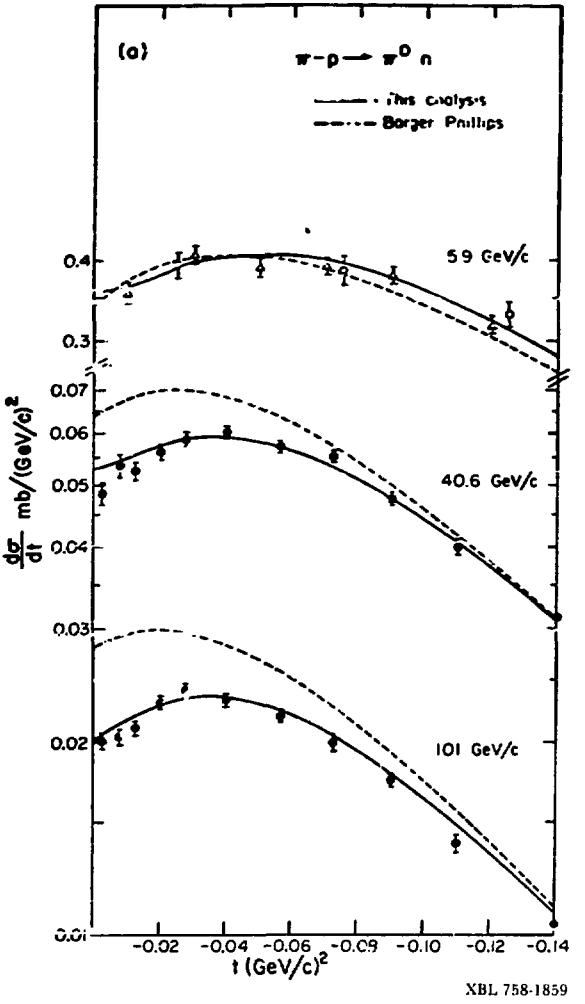
(a)
π⁻p → π⁰n
This analysis
Berger Phillips
5.9 GeV/c
40.6 GeV/c
101 GeV/c
dσ/dt mb/(GeV/c)²
0.4
0.3
0.07
0.06
0.05
0.04
0.03
0.02
0.01
-0.02
-0.04
-0.06
-0.08
-0.10
-0.12
-0.14
t (GeV/c)²
XBL 758-1859

Fig. 14

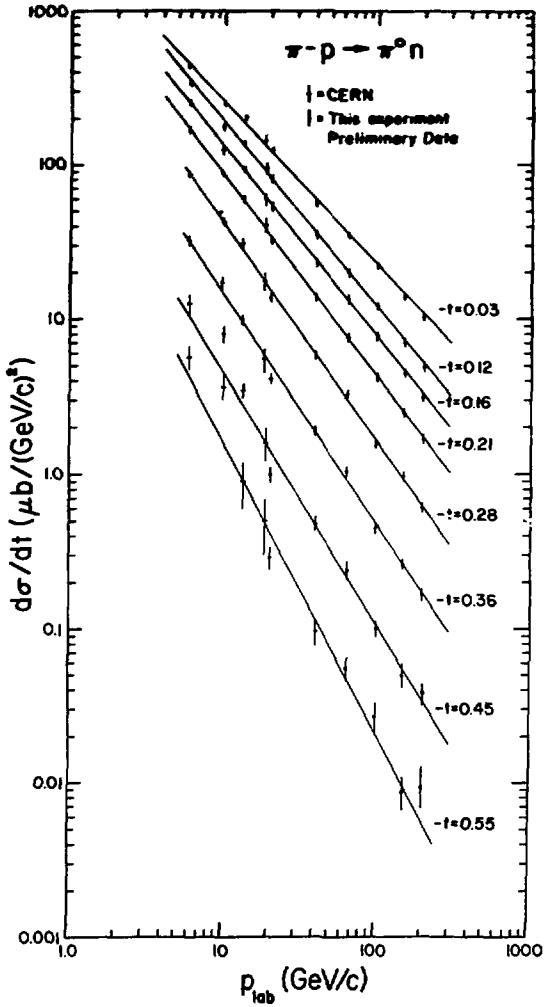

XBL 756-1516A

Fig. 15

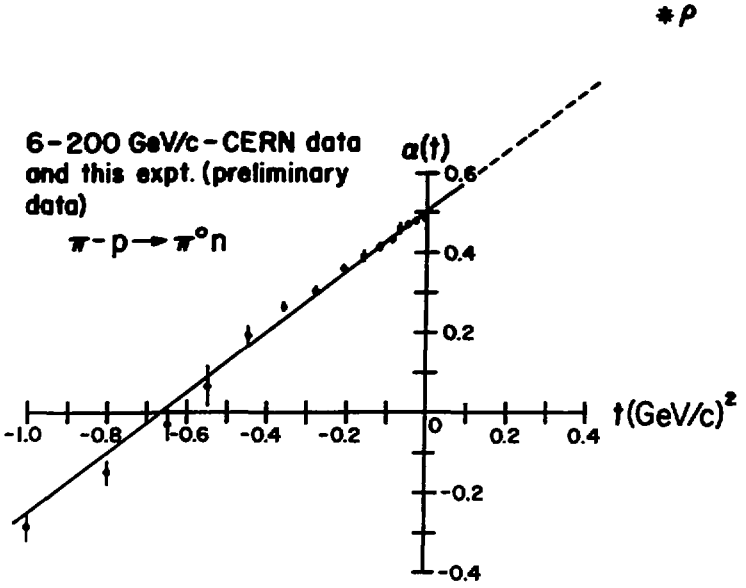

EFFECTIVE TRAJECTORY

NBL 757-1846

Fig. 16

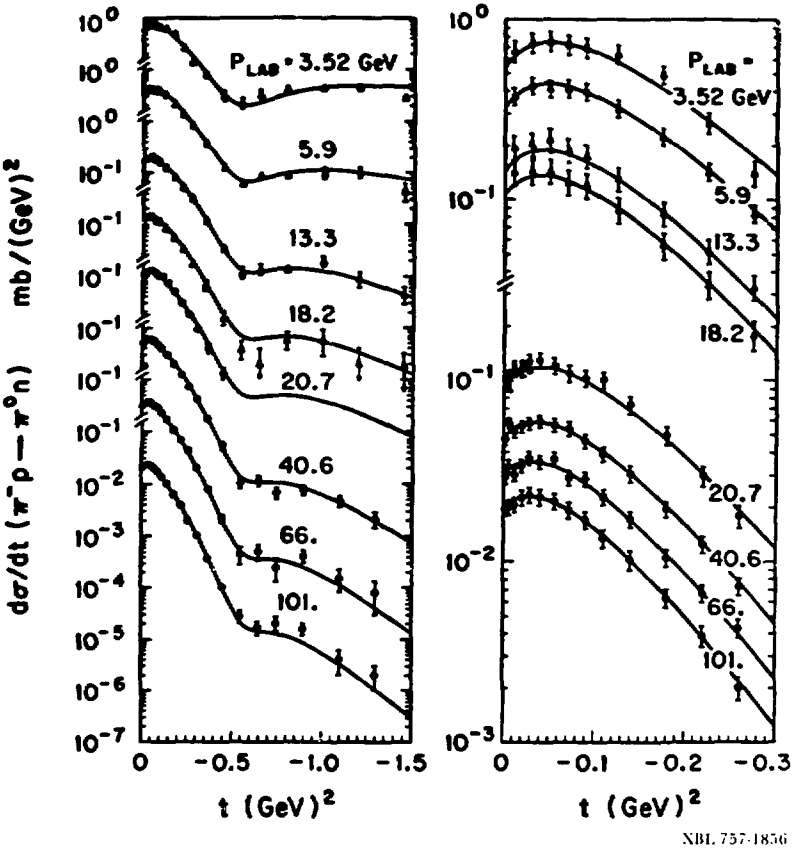

XBL 757-1856

Fig. 17

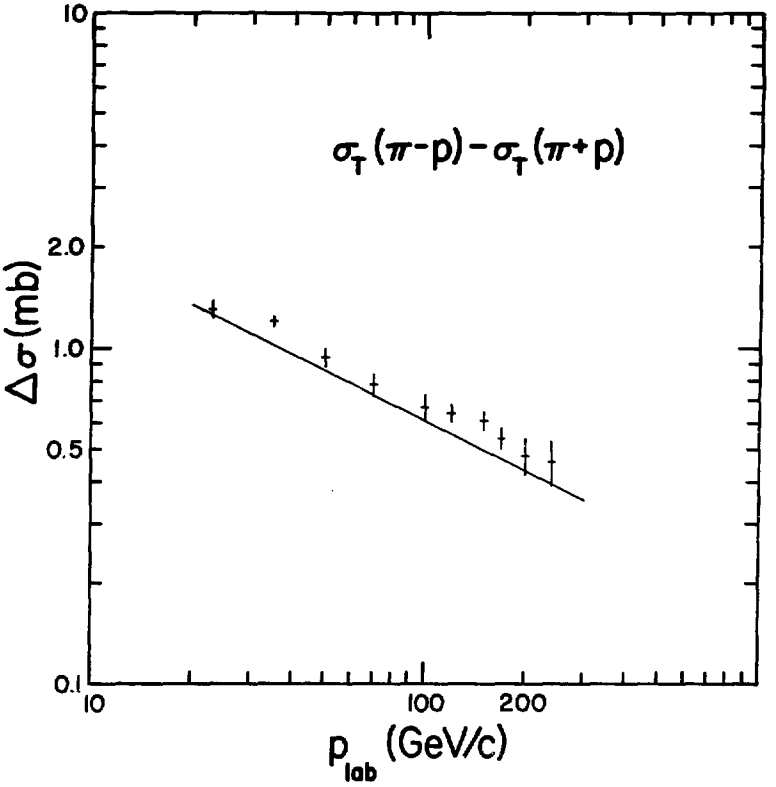

NBL 756-1511A

Fig. 18

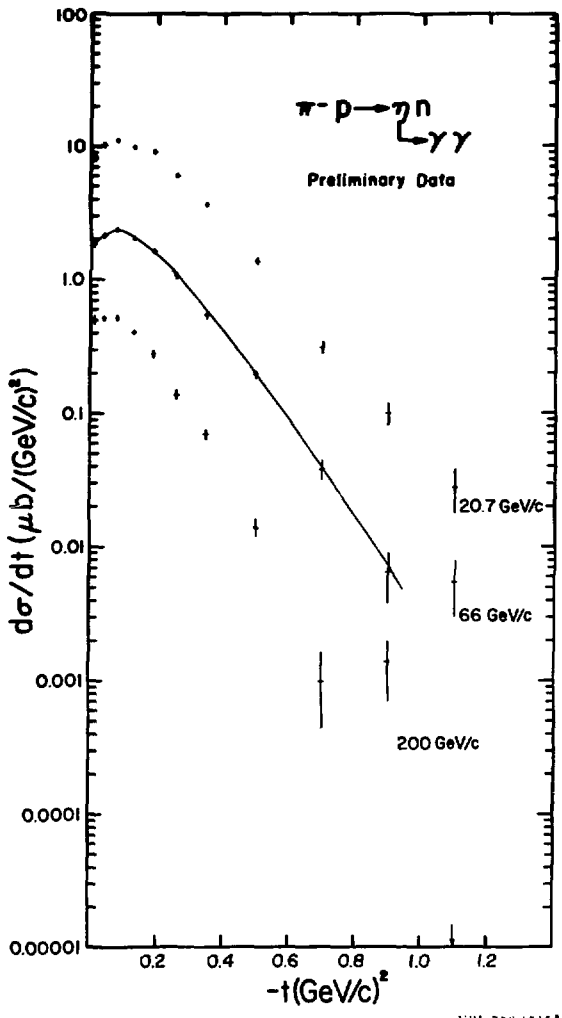
$\pi^- p \to \eta n$
$\eta \to \gamma\gamma$
Preliminary Data
20.7 GeV/c
66 GeV/c
200 GeV/c
$d\sigma/dt\ (\mu b/(GeV/c)^2)$
$-t(GeV/c)^2$
100
10
1.0
0.1
0.01
0.001
0.0001
0.00001
0.2
0.4
0.6
0.8
1.0
1.2
XBL 756-1515A

Fig. 19

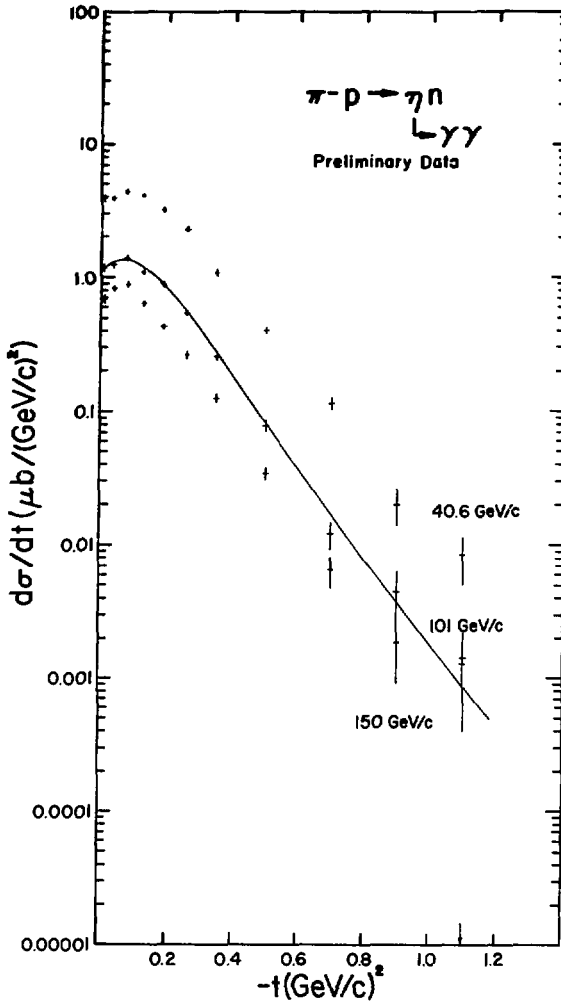
$\pi^- p \to \eta n$
$\hookrightarrow \gamma\gamma$
Preliminary Data
40.6 GeV/c
101 GeV/c
150 GeV/c
$d\sigma/dt\ (\mu b/(GeV/c)^2)$
$-t(GeV/c)^2$
100
10
1.0
0.1
0.01
0.001
0.0001
0.00001
0.2
0.4
0.6
0.8
1.0
1.2
XBL 756-1519A

Fig. 20

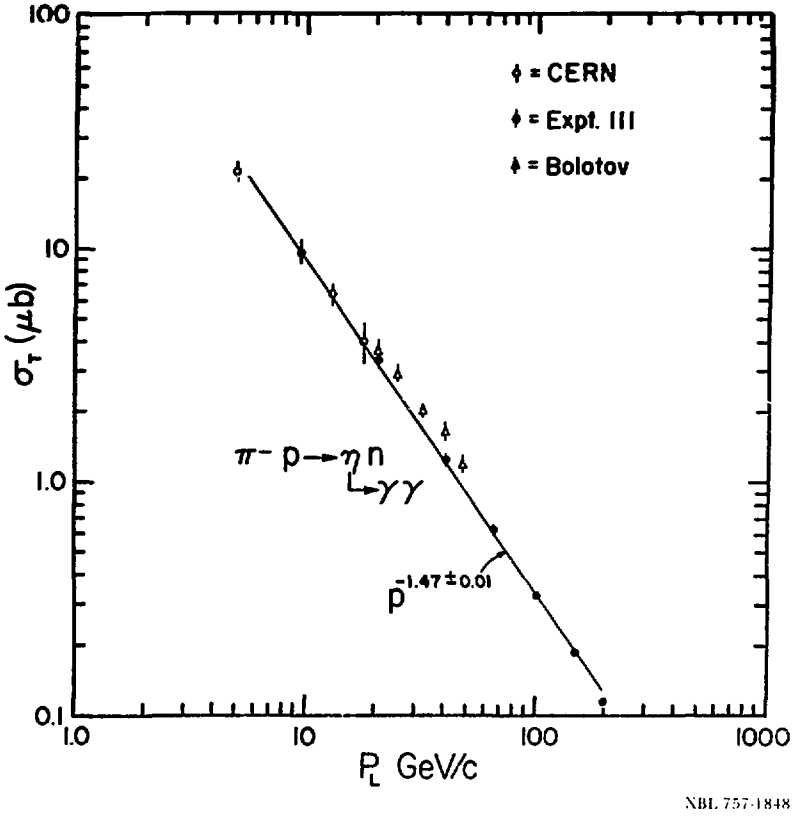
100
10
1.0
0.1
1.0
10
100
1000
σ_T (μb)
P_L GeV/c
= CERN
= Expt. 111
= Bolotov
$\pi^- p \rightarrow \eta n$
$\eta \rightarrow \gamma\gamma$
$p^{-1.47 \pm 0.01}$
NBL 757-1848

Fig. 21

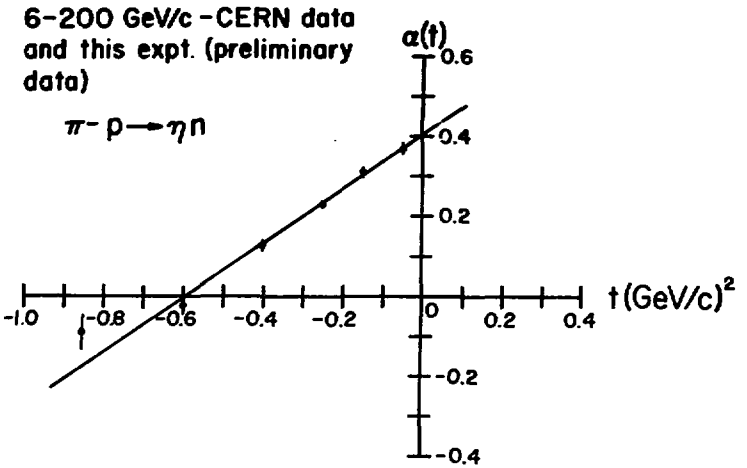

EFFECTIVE TRAJECTORY

NBL 756-1514 A

Fig. 22

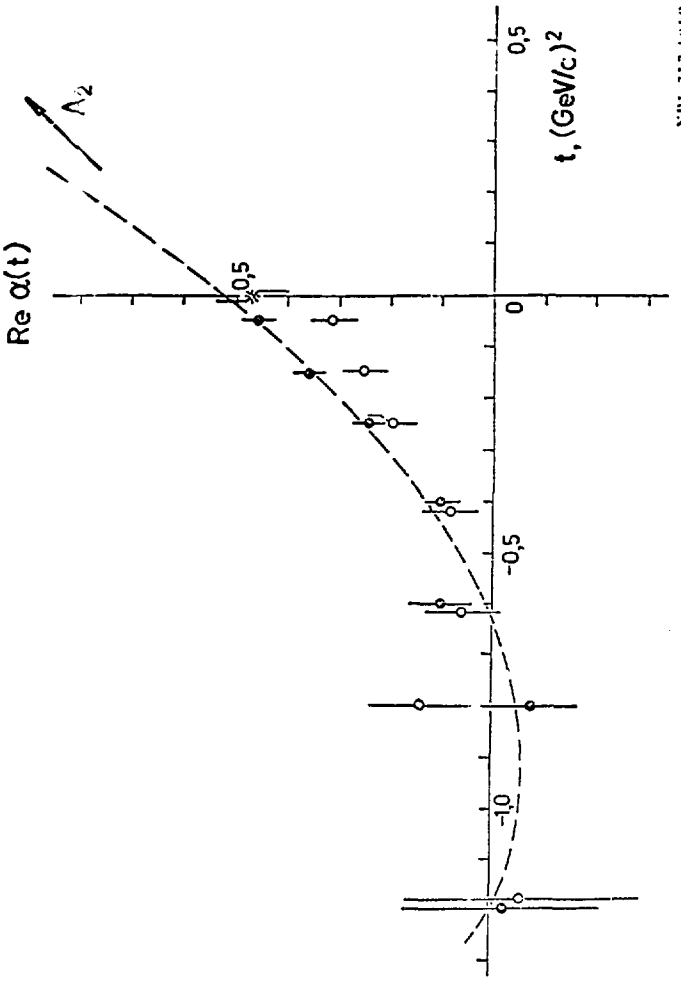

Fig. 23

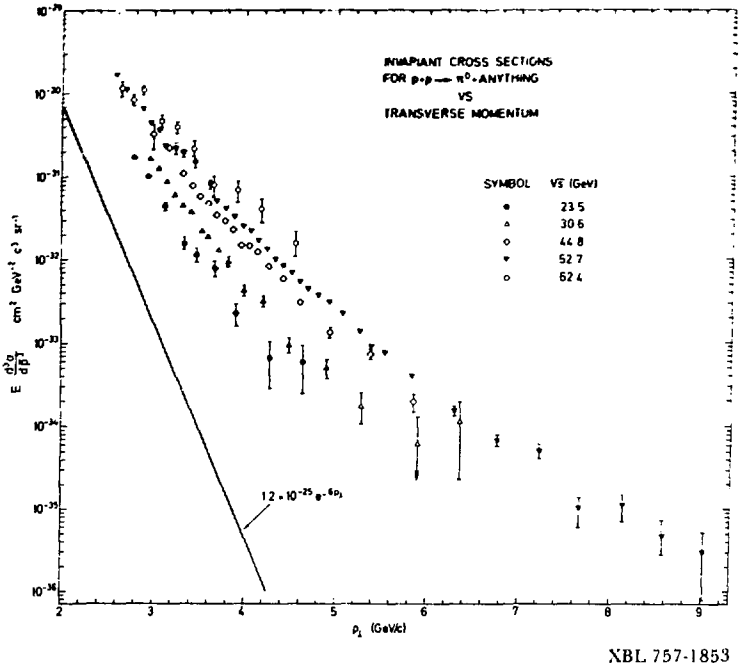

XBL 757-1853

Fig. 24

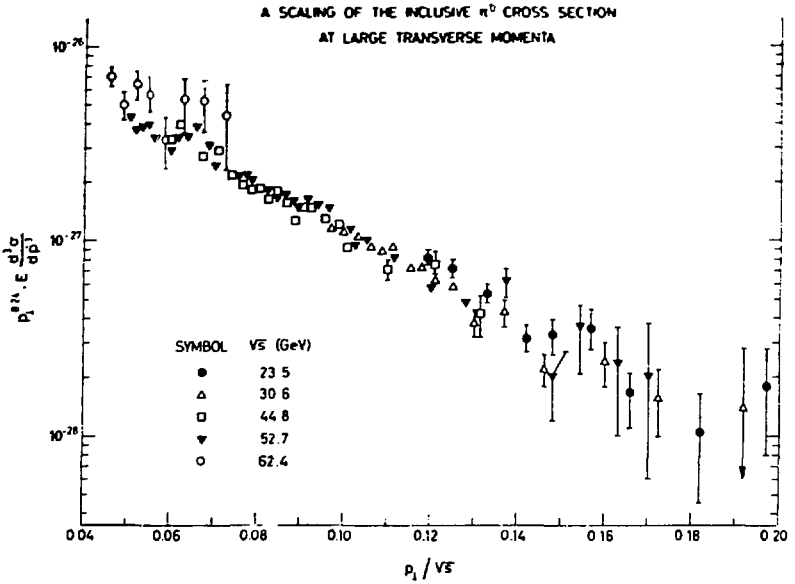

XBL 757-1854

Fig. 25

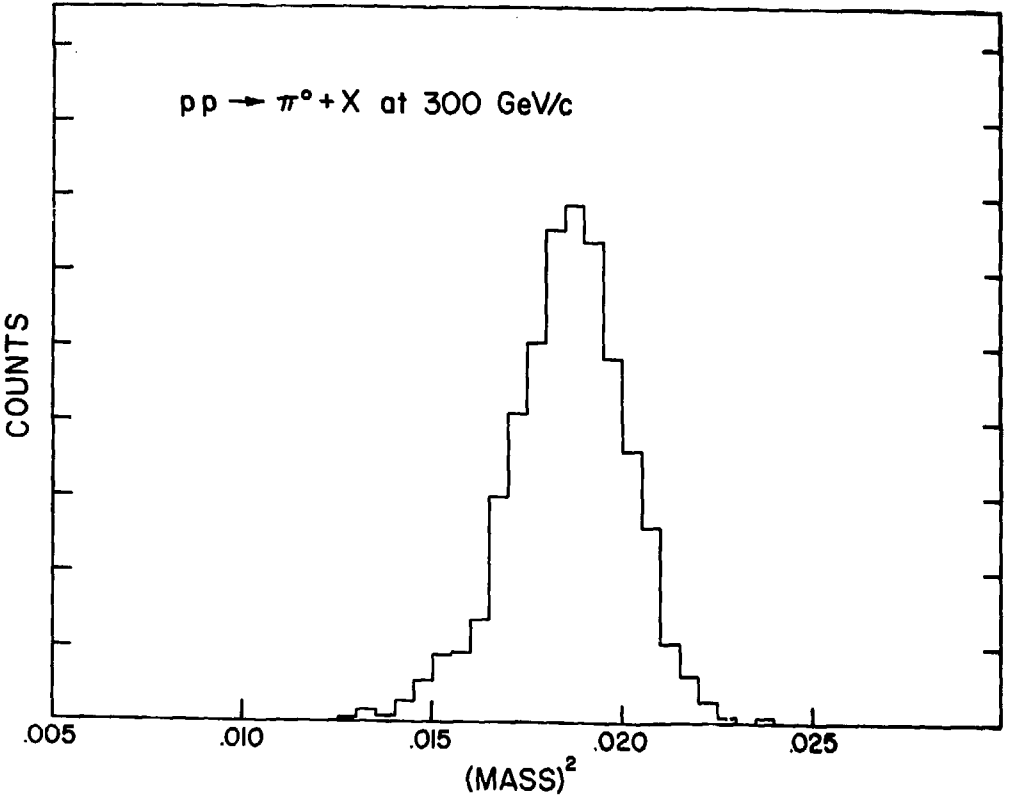

XBL 758-1862

Fig. 26

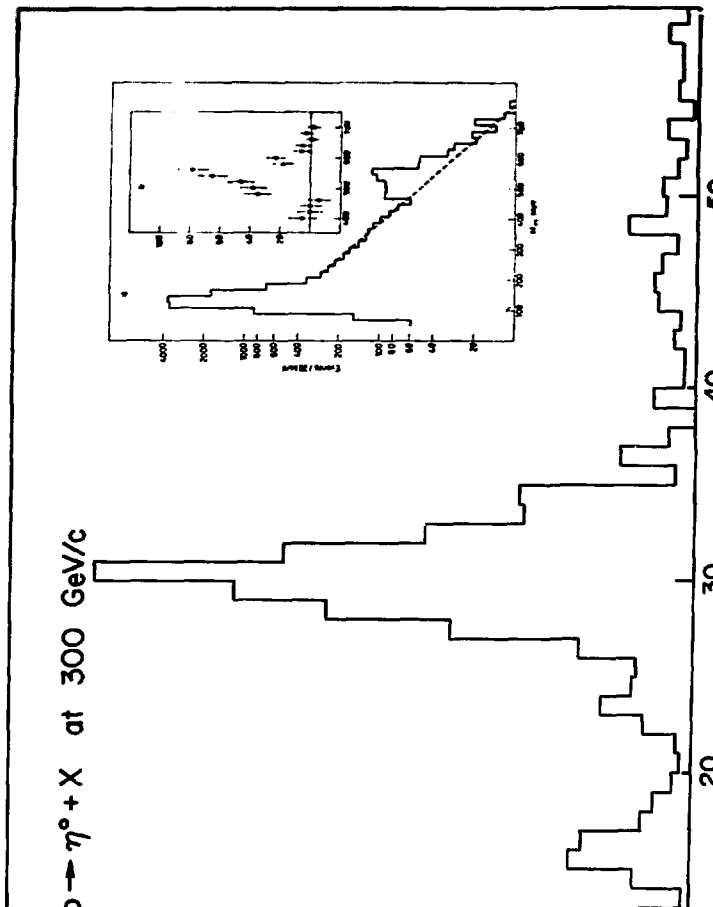

NBL 758-1861

Fig. 27